ELSEVIER

Journal of Chromatography A, 764 (1997) 3–20

JOURNAL OF CHROMATOGRAPHY A

Mass transfer limitations in protein separations using ion-exchange membranes

Frank T. Sarfert[a], Mark R. Etzel[a,b,*]

[a]*Department of Chemical Engineering, 1415 Engineering Drive, University of Wisconsin, Madison, WI 53706, USA*
[b]*Department of Food Science, 1605 Linden Drive, University of Wisconsin, Madison, WI 53706, USA*

Received 25 June 1996; revised 16 September 1996; accepted 16 October 1996

Abstract

Sorption of bovine serum albumin to commercial 150-μm pore size membranes was measured in batch and flow experiments. For residence times of 2–40 min, early and broad breakthrough curves and broad asymmetric elution peaks were observed that depended strongly on flow-rate. System dispersion could not explain the flow-rate dependence. Breakthrough and elution curves were analyzed using new models that included Langmuir sorption, convection and diffusion. From the analysis, film mass transfer resistance was found to be the rate-limiting factor. The maximum allowable pore size that eliminates this limitation was calculated for different molecular weight solutes.

Keywords: Membrane; Mass transfer resistance; Ion-exchange membrane; Adsorption isotherm; Protein

1. Introduction

Ion-exchange membranes were developed to overcome the limitations encountered in conventional commercial processes using beads [1–4]. For beads, the rate of adsorption is controlled by external diffusion of protein to the bead surface (film mass transfer), or internal diffusion of protein to the adsorption site (solid-phase diffusion). Beads can be made smaller to increase diffusion rates, but this increases resistance to flow. For ion-exchange membranes, the protein solution flows through the pores of the membranes. Therefore, protein is transported into the membrane structure by convection. Pressure drop limitations are negligible if the membranes are made thin. Consequently, properly designed and operated ion-exchange membrane separations may outperform bead-based separations in the isolation of proteins from dilute protein solutions.

Originally, ion-exchange membranes were sold as single thin sheets having pore sizes on the order of 1 μm. However, the capacity of these membranes was low, and small thickness and porosity variations severely degraded membrane performance [2,3,5]. Furthermore, in practice, when these membranes were used to separate proteins from crude solutions, suspended solids, lipids and aggregated proteins plugged the membrane pores [6].

The next generation of ion-exchange membranes consisted of stacks of individual membranes [2,3,7]. This solved the problems of low capacity and poor performance. The problem of plugging persisted. Performance was nearly ideal, wherein breakthrough curves were qualitatively consistent with predictions from local-equilibrium theory [4]. In general, there was a remarkable absence of flow-rate effects on the

*Corresponding author.

PII S0021-9673(96)00894-1

breakthrough curves due to the absence of mass transfer limitations [4,8]. In one exception, Shiosaki et al. [9] found that breakthrough curves for ovalbumin (46 kDa) were dependent on flow-rate, while those for the smaller myoglobin (18 kDa) were not.

The newest generation of ion-exchange membranes consists of stacks of individual membranes each having a pore size on the order of ten to several hundred micrometers [6,10]. This solves the problems of low capacity, poor performance and plugging. However, in order for protein to bind, the residence time of the liquid in the membrane (L/v) must greatly exceed the time scale (t_{film}) for mass transfer through the film to the pore wall, and diffusion into the pore wall (if the wall is porous). As an order of magnitude approximation, $t_{film}=d_p^2/4D$, where d_p is the membrane pore size and D is the diffusion coefficient of the protein. As the pore size is increased, very quickly the pores are too large for protein to reach the pore wall by diffusion before passing through the membrane, decreasing protein recovery [10]. Consequently, it is a very important design issue to determine the appropriate pore size for a given application that balances mass transfer limitations for pores that are too large against plugging for pores that are too small.

The elution peak is frequently the product, or close to the final product, in a protein production process. Completeness of protein removal impacts final yield and long-term membrane capacity. Speed of protein removal impacts the throughput of the process. Concentration of protein in the elution peak impacts the cost of downstream processing. Although neglected in the past, experimental and mathematical characterization of the elution curve is of utmost importance to the success of ion-exchange separations in industry. Flow-rate affects the shape of the elution curve for recovery of bound bovine IgG from recombinant protein G affinity membranes [11]. However, these phenomena have not previously been investigated for ion-exchange membranes, and will be of little general value unless a mathematical model is developed that can accurately predict the precise influence of system parameters such as pore size, flow-rate, and solute molecular size on performance.

The objectives of this work were to: (1) measure the effect of flow-rate on the elution and breakthrough curves for separation of bovine serum albumin from dilute solution using a large pore-size ion-exchange membrane, (2) for both the breakthrough and the elution curves, develop mathematical models that include convection, Langmuir adsorption, mass transfer resistance, and dispersion in the flow system, (3) use the models to analyze the data and determine the fundamental phenomena controlling system performance, and (4) calculate the tradeoffs between pore size and flow-rate in the design and operation of ion-exchange membrane separations.

2. Experimental

2.1. Materials

Experiments were performed using an S-type ion-exchange membrane cartridge (PSC10-SP, Metachem Technologies, Torrance, CA, USA), with an average pore size of 150 μm. Five stacks of interwoven membrane material made of regenerated cellulose were sealed in a 25×20-mm cylindrical, acrylic housing. A system of radial channels in the top and bottom lid of the housing distributed the flow at the entrance and exit of the cartridge, respectively.

Bovine serum albumin (BSA) monomer (66.3 kDa) was purchased from Sigma (A-0161, *S*-cysteinyl–albumin, St. Louis, MO, USA). It was compared to an ICN product (810–281, Costa Mesa, CA, USA) having a known monomer content of 96.6%. Size exclusion HPLC analysis revealed an even lower dimer content for the Sigma product (data not shown) [12]. The peptide tyrosine–glycine–glycine (TGG) was obtained from Sigma (T-9005).

The buffer used in the loading and washing stage (L/W buffer) was 0.1 *M* sodium citrate–citric acid pH 3.0. The elution buffer was 1 *M* NaCl in L/W buffer. All buffers were filtered through 0.45-μm Gelman Sciences microfilters (Supor-450, Model 60173, Ann Arbor, MI, USA) and vacuum degassed prior to use. The concentration of all feed solutions was determined from the absorbance at 280 nm, using an extinction coefficient of 6.3 ml/(mg cm). Sodium azide (0.01% wt/wt) was added to the protein solution after filtration to avoid bacterial growth in experiments running longer than 36 h.

2.2. Sorption isotherm

Membranes were cleaned by sequential flushing with 0.2 *M* NaOH, deionized water, 0.2 *M* HCl and deionized water [12]. The final flush continued until the pH was greater than 6. Membranes were regenerated just prior to use by flushing with 100 ml of elution buffer followed by 100 ml of L/W buffer.

Wet membrane segments were incubated in a clean glass beaker containing 50 ml of protein solution of known concentration. The beaker was covered and placed on a shaker at 200 rpm for 48 h, at which point the protein concentration in the liquid was determined spectroscopically.

The results from these experiments were reproducible for initial protein concentrations less than 0.1 mg/ml, but were not adequately reproducible for concentrations greater than 0.1 mg/ml. Therefore, results in the higher concentration range were supplemented by results obtained from recirculating flow experiments. The setup consisted of a glass beaker, a metering pump (Model 7520-25, Cole-Parmer, Chicago, IL, USA) with a zero dead-volume pump head (RH0CKC, Fluid Metering, Oyster Bay, NY, USA), the membrane cartridge, and the 10-mm path-length flow cell of an absorbance detector (UA-5 with Type 6 optical unit, ISCO, Lincoln, NE, USA). Upon start-up, 50 ml of the initial protein solution were recirculated at a constant flow-rate of 1.0 ml/min until no further binding of protein to the membrane could be detected, up to 48 h. For subsequent data points, 10 ml of the equilibrated protein solution were removed for analysis after equilibrium was attained and replaced by 10 ml of feed solution at a greater protein concentration. After stirring the solution for 5 min, the pump was restarted and the liquid was recirculated until equilibration was achieved. Protein concentration was calculated from the spectrophotometric absorbance.

2.3. Flow experiments

The setup for the flow experiments was similar to the setup described in the preceding section. To minimize dead volume, the liquid was pumped through PTFE capillary tubing (0.8-mm inside diameter) to the cartridge and the flow cell. Tubing length was minimized where possible. Absorbance readings were recorded using a datalogger (Model 50, Electronic Controls Design, Milwaukie, OR, USA) and transferred to a personal computer for further analysis. All experiments were performed at 21°C. Prior to all experiments, the system (i.e. tubing, fittings, cartridge, pump head, flow cell) was cleared of trapped air. Flow-rates (5.0, 1.0 and 0.2 ml/min) were measured by collecting the effluent volume over a time period of approximately 5 min.

2.4. System dispersion curves

To serve as the tracer material, 0.5 g of TGG were dissolved in 1.0 l of elution buffer. Adsorption of TGG to the membrane was precluded by the large excess of NaCl in the elution buffer. TGG instead of BSA was chosen as tracer material because of its low affinity and good solubility in solutions of high ionic strength. The membrane was cleaned and equilibrated, the baseline absorbance was set using the L/W buffer, and the flow-rate was measured prior to all experiments. At zero time, the pump was started and the feed solution containing TGG as tracer entered the system at a constant flow-rate. Pumping continued beyond breakthrough until a steady state was achieved. Next, washing buffer was pumped through the system until the absorbance returned to the baseline. The membrane cartridge was taken out of the system, and feed solution was pumped through the flow cell to measure the absorbance for later normalization of the absorbance values.

2.5. Breakthrough and elution curves

For breakthrough curve (BTC) and elution curve (EC) measurements, a feed solution of 2.75 ± 0.05 g BSA per liter of buffer was utilized ($4.15 \pm 0.075 \times 10^{-5}$ *M*). The procedure consisted of several steps. The membrane was flushed with L/W buffer to equilibrate it, adjust the baseline absorbance to zero, and to determine the flow-rate. For loading, 75 ml of feed solution were pumped through the membrane. The membrane was then flushed with approximately 50 ml of L/W buffer until the effluent absorbance returned to baseline. Elution buffer (approximately 50 ml) was pumped through the membrane until the effluent absorbance returned to baseline. Lastly, the

membrane was flushed with L/W buffer (approximately 25 ml) until the absorbance returned to baseline. After disconnecting the membrane, the absorbance of the feed solution was measured for use in calibration of the results.

3. Theoretical

3.1. Breakthrough curve model

The mass balance over the membrane is given by [5,13]

$$\underset{\text{unsteady state}}{\varepsilon\frac{\partial c}{\partial t}} + \underset{\text{convection}}{\varepsilon v\frac{\partial c}{\partial z}} = \underset{\text{axial dispersion}}{\varepsilon\xi\frac{\partial^2 c}{\partial z^2}} - \underset{\text{adsorption}}{(1-\varepsilon)\frac{\partial c_s}{\partial t}} \quad (1)$$

For axial dispersion Peclet numbers (Pe_ξ) greater than 40, axial dispersion is negligible for adsorptive membranes [5]. In this work, $Pe_\xi = 211$ to 125 for $v = 9.05\times10^{-4}$ to 2.26×10^{-2} cm/s, respectively. Therefore, it is valid to neglect the axial dispersion term in Eq. (1).

Transport of solute from the liquid to the solid phase involves diffusion through the boundary layer, diffusion into the solid phase, and sorption to the binding sites. These transport processes were described using an overall mass transfer coefficient [14,15]

$$\frac{\partial c_s}{\partial t} = k_{ol}a_m(c - c^*), \quad (2)$$

where a_m is the ratio of internal surface area to solid polymer volume, k_{ol} is the overall liquid-phase mass transfer coefficient, and c^* denotes the fictitious solute concentration in the liquid phase in equilibrium with c_s.

The Langmuir isotherm

$$c_s = \frac{c_1 c^*}{K_d + c^*} \quad (3)$$

for a flow system at complete saturation ($c = c_o$ everywhere in the pores), simplifies to

$$c_s^\infty = \frac{c_1 c_o}{K_d + c_o} \quad (4)$$

Using Eq. (4) to substitute for the membrane capacity c_1 in Eq. (3) yields

$$c^* = \frac{c_o c_s K_d}{c_s^\infty(K_d + c_o) - c_o c_s}, \quad (5)$$

where the liquid phase concentration c_o is in equilibrium with the solid-phase concentration c_s^∞, and K_d denotes the desorption equilibrium constant. Eq. (2) can be solved by substituting in Eq. (5).

Thomas [16,17] derived the analytical solution for a mass balance without the axial dispersion term coupled with a second-order rate expression. This solution has been generalized [18] and applied to a variety of similar problems. Use of the Thomas solution requires the following dimensionless variables

$$T_L = (\tau - \zeta)\frac{n}{m}\frac{r}{r + C_s - rC_s} \quad (6)$$

$$Z_L = \zeta n \frac{r}{r + C_s - rC_s}. \quad (7)$$

Applying the above variable transformations (Eqs. (6,7)), the mass balance (Eq. (1)) reduces to [12]

$$\frac{\partial C}{\partial Z_L} + \frac{\partial C_s}{\partial T_L} = 0, \quad (8)$$

and the rate expression (Eq. (2)) to

$$\frac{\partial C_s}{\partial T_L} = C[1 - C_s] - \frac{1}{r}C_s[1 - C] \quad (9)$$

The boundary and initial conditions are

$$C = 1 \text{ at } Z_L = 0, T_L > 0 \quad (10)$$

$$C = 0 \text{ at } Z_L \geq 0, T_L = 0 \quad (11)$$

$$C_s = 0 \text{ at } Z_L \geq 0, T_L = 0 \quad (12)$$

For this system of differential equations (Eqs. (8–12)), the following solution holds [16–18]

$$C = \frac{J\left(\frac{Z_L}{r}, T_L\right)}{J\left(\frac{Z_L}{r}, T_L\right) + \left[1 - J\left(Z_L, \frac{T_L}{r}\right)\right]\exp\left[\left(\frac{1}{r} - 1\right)(T_L - Z_L)\right]} \quad (13)$$

with

$$J(\alpha,\beta) = 1 - \int_0^{\alpha} \exp(-\beta - \eta) I_0(2\sqrt{\beta\eta})\, d\eta \qquad (14)$$

where I_0 is the modified Bessel function of zeroth order and η is an integration variable. The assumption of $C_s = 0.5$ by Hiester and Vermeulen [18] was used to simplify Eqs. (6,7), converting the Thomas solution into an explicit form.

3.2. Elution curve model

Analogous to the breakthrough curve, the mass balance is

$$\varepsilon \frac{\partial c}{\partial t} + \varepsilon v \frac{\partial c}{\partial z} = -(1-\varepsilon)\frac{\partial c_s}{\partial t} \qquad (15)$$

In order to write the mass balance in dimensionless form, it is useful to define the contact time θ, i.e. the time the membrane at position z is in contact wth the incoming fluid in plug flow [19]

$$\theta = \frac{vt}{L} - \frac{z}{L} \qquad (16)$$

If loading continues until the membrane attains complete saturation, the solid-phase concentration is everywhere equal to c_s^{∞}. However, the elution curve represents only the mass of protein that adsorbed to the membrane and subsequently desorbed, which can be determined by integrating the area under the elution curve. Dividing this mass by the membrane solid volume yields the average desorbable protein concentration $c_{s,EC}^{int}$. Therefore, it is appropriate to substitute $c_{s,EC}^{int}$ for c_s^{∞}. Consequently, the following different definitions were used for the dimensionless solute concentration in the solid-phase

$$C_s = \frac{c_s}{c_{s,EC}^{int}} \qquad (17)$$

and the dimensionless saturation capacity

$$m = \frac{(1-\varepsilon)c_{s,EC}^{int}}{\varepsilon c_0} \qquad (18)$$

Using these definitions, the mass balance (Eq. (15)) simplifies to [12]

$$\frac{\partial C}{\partial \zeta} + m\frac{\partial C_s}{\partial \theta} = 0 \qquad (19)$$

The boundary and initial conditions are

$$C = 0 \text{ at } \zeta = 0, \theta > 0 \qquad (20)$$

$$C = 0 \text{ at } \zeta \geq 0, \theta = 0 \qquad (21)$$

Two main assumptions were used in the formulation of the rate expression for the elution stage. First, when the elution buffer contacts the membrane, the binding interaction is completely and instantaneously disrupted. Mathematically, this assumption results in the desorption equilibrium constant approaching infinity, thus simplifying the equation for the Langmuir isotherm (Eq. (3))

$$\lim_{K_d \to \infty} c_s^* = \lim_{K_d \to \infty} \left(\frac{c_l c}{K_d + c} \right) = 0 \qquad (22)$$

Second, an overall solid-phase mass transfer coefficient is defined as

$$\frac{\partial c_s}{\partial t} = k_{os} a_m (c_s^* - c_s) \qquad (23)$$

The combination of Eqs. (22,23) yields the rate expression for elution

$$\frac{\partial c_s}{\partial t} = -k_{os} a_m c_s \qquad (24)$$

Using dimensionless variables, Eq. (24) simplifies to

$$\frac{\partial C_s}{\partial \theta} = -\frac{\varepsilon}{1-\varepsilon} n C_s \qquad (25)$$

The initial condition is

$$C_s = 1 \text{ at } \zeta \geq 0, \theta = 0 \qquad (26)$$

Assuming piecewise differentiability of $C = C(\zeta, \theta)$ and $C_s = C_s(\zeta, \theta)$, the solution to the model equation is [12]

$$C = \begin{cases} 0 \text{ at } \theta \leq 0, 0 \leq \zeta \leq 1 \\ \dfrac{\varepsilon}{1-\varepsilon} nm\zeta \exp\left(-\dfrac{\varepsilon}{1-\varepsilon} n\theta \right) \text{ at } \theta > 0, \quad 0 \leq \zeta \leq 1. \end{cases} \qquad (27)$$

3.3. System dispersion curve model

A system dispersion model was used to describe the effects of flow non-idealities such as mixing, channeling and dead volume. The model accounts for the entire flow system, i.e. it is defined with

respect to the system volume V_{sys}. Apart from the membrane void volume V_{void}, the system volume also entails the external volume V_{ext} consisting of the volume of tubing and fittings, the volume of flow distributors, the volume of the detector flow cell, and the volume of the pump head. Thus,

$$V_{sys} = V_{void} + V_{ext} \tag{28}$$

A simple but sufficiently accurate model to describe the flow behavior is the serial combination of an ideal continuously stirred tank region (CSTR) and an ideal plug flow region (PFR). Hence broadening of the step response is understood as the contribution of the CSTR portion of the system to the overall behavior, whereas time delay in the step response is assigned to the PFR portion of the system. Therefore,

$$V_{sys} = V_{CSTR} + V_{PFR} \tag{29}$$

where V_{CSTR} denotes the CSTR volume and V_{PFR} the PFR volume.

The model equation for the CSTR is [13]

$$\frac{dc_{out}}{dt} = \frac{Q}{V_{CSTR}} [c_{in} - c_{out}] \tag{30}$$

where c_{in} denotes the influent and c_{out} the effluent concentration, and where Q is the volumetric flow-rate. The initial condition is

$$C_{out} = 0 \text{ at } t = 0 \tag{31}$$

The PFR is represented as

$$c_{out}(t) = \begin{cases} 0 & \text{for } t < t_{delay} \\ c_{in}(t - t_{delay}) & \text{for } t \geq t_{delay} \end{cases} \tag{32}$$

where the delay time t_{delay} is due to the PFR volume, which shifts the response to longer times within $0 \leq t_{delay} \leq t_{sys}$.

The response of either the breakthrough or elution model was used as the influent concentration for the CSTR model. The CSTR response was used as the influent concentration for the PFR model. The PFR response, then, represents the system response.

The breakthrough curve of a non-binding solute is also called the system dispersion curve (SDC) because it characterizes the dispersive (flow) behavior of the system independent of the effects of binding mechanisms. The SDC at each flow-rate was measured and used to calculate the mean residence time $\bar{t}$ from [20,21]

$$\bar{t} = \frac{M_1 - \mu_1}{M_0}, \tag{33}$$

where M is the moment of the effluent concentration and μ is the moment of the inlet concentration. Finally, the system volume was calculated from

$$V_{sys} = Q\bar{t} \tag{34}$$

For the special case of the SDC, a simple expression for the CSTR model (Eq. (30)) was derived for a step increase in the influent concentration c_{in} from 0 to c_0. It was combined with the PFR model (Eq. (32)) to yield

$$c_{out}(t) = \begin{cases} 0 & t < t_{delay} \\ c_0\left(1 - \exp\left[-\frac{Q}{V_{CSTR}}(t - t_{delay})\right]\right) & t \geq t_{delay} \end{cases} \tag{35}$$

The system dispersion model (Eq. (35)) was fit to the SDCs using the general regression software package GREG [22]. The fitting parameter was V_{CSTR} with the constraint $0 \leq V_{CSTR} \leq V_{sys}$. The value for V_{PFR} was calculated from Eq. (29).

4. Results

4.1. Membrane morphology

The morphology of the microporous ion-exchange membrane was examined using scanning electron microscopy at different magnifications and viewpoints. The plan view photomicrographs (Fig. 1A,B) reveal the highly porous structure of the face of the membrane as well as the wide variation of pore sizes. Macropores occur in the size range of 50 to 300 μm, close to the average value of 150 μm reported by the manufacturer. Neither a linear path through the membrane nor the presence of cylindrical channels is apparent. Instead, all visible paths through the membrane follow a twisted tortuous trajectory, passing abruptly through large and small macropores in succession, with frequent sudden changes in direction.

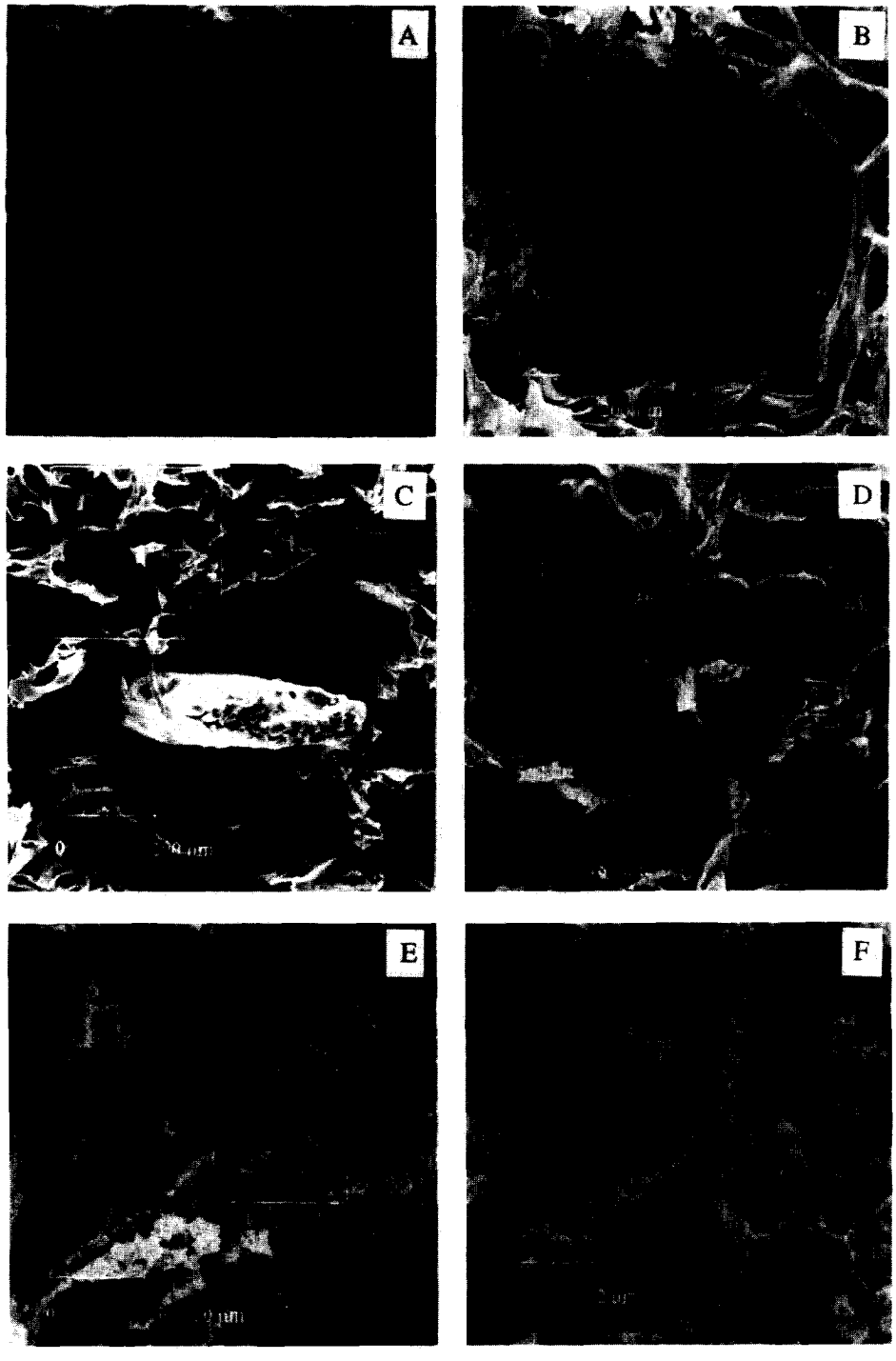

Fig. 1. Morphology of the microporous membrane from scanning electron microscopy.

A stepwise enlargement of an edge view of one of the membrane segments is shown in Fig. 1C–F. The enlarged areas are indicated by white framed squares. As illustrated in Fig. 1C, the membranes consist of a continuous sponge-like structure sparsely interspersed by solid support fibers that extend parallel to the front face of the membrane. The membrane matrix itself consists of numerous lamellae of random orientation. Macropores result from holes in the lamellae and from plate-like sheets that abut at angles. Although at low magnification the lamellae appear to consist of smooth tight walls (Fig. 1C), upon closer examination a structure is revealed (Fig. 1D,F) wherein the regenerated cellulose base-matrix is permeated by fine (0.5 μm) micropores.

4.2. Sorption isotherm

The sorption isotherm was measured at 21°C by two methods. First, for low concentrations, membrane segments were incubated with protein solution in a beaker. Second, for high concentrations, protein solution was recirculated through the membrane cartridge. A least squares fit of the Langmuir isotherm equation (Eq. (3)) to the experimental data (Fig. 2) yielded $c_1 = 2.4 \pm 0.4 \times 10^{-3}$ M and $K_d = 5.5 \pm 0.9 \times 10^{-7}$ M (mean ± standard error). Consequently, at the feed solution concentration ($c_0 = 4.15 \times 10^{-5}$ M), the membrane sites were fully occupied ($c_s^{\infty} \approx c_1$) when the flow system attained equilibrium.

Independent determination of the maximum binding capacity was possible by calculating the total amount of bound protein in the flow experiments. The mass of protein passing through the membrane that was not captured during the loading stage was calculated by integrating under the BTC and washing curve. Subtracting this value from the mass of protein loaded and dividing by the membrane solid volume gives the average concentration of bound protein $c_{s,\mathrm{BTC-WC}}^{\mathrm{int}}$, which was 2.7×10^{-3}, 1.7×10^{-3} and 0.9×10^{-3} M at flow-rates of 0.2, 1.0 and 5.0 ml/min, respectively. Loading was stopped before complete saturation of the membrane in these experiments. However, at the lowest flow-rate the system was probably closest to saturation, and this calculated concentration of bound protein was equal to c_1, determined separately in the isotherm experiments, within experimental error.

4.3. Analysis of the system dispersion curves

The SDC was measured in triplicate at each of three different flow-rates, and the average result was plotted in Fig. 3. The effect of flow-rate variation

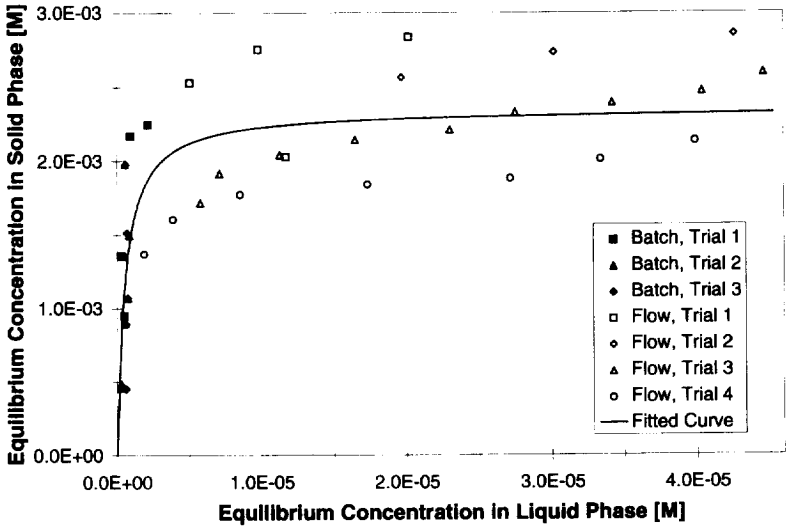

Fig. 2. Adsorption isotherm of BSA in 0.1 M citrate buffer pH 3.0 to an S-type ion exchange membrane and the fit of the Langmuir isotherm to the data.

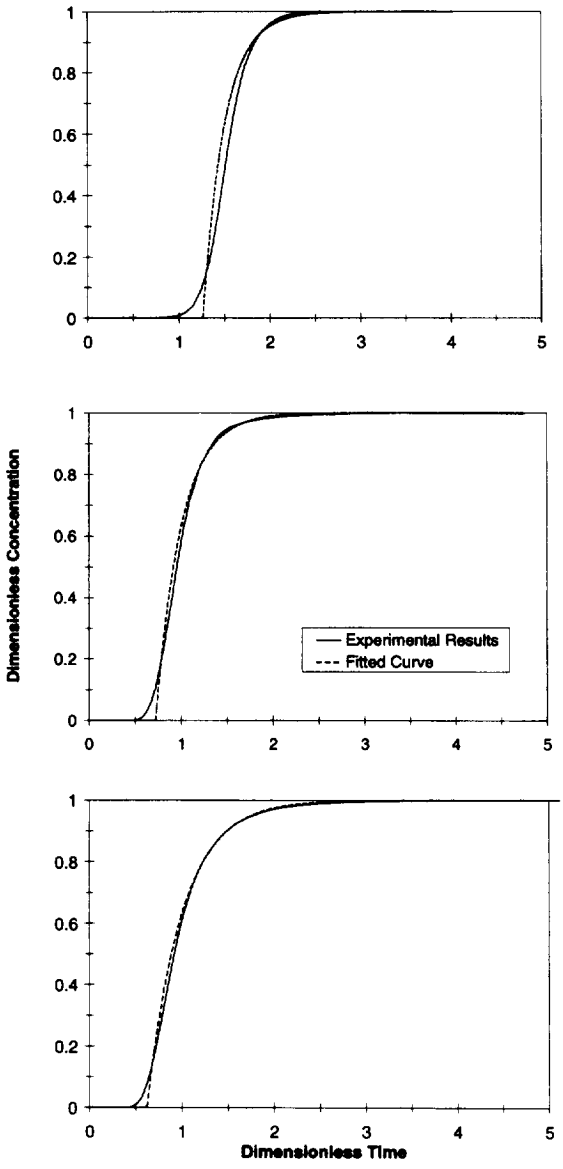

Fig. 3. Experimental system dispersion curves (solid line) and fitted curve for the mixing model (dotted line) at flow-rates of 0.2 ml/min (top panel), 1.0 ml/min (middle panel) and 5.0 ml/min (bottom panel).

was perceptible but not pronounced. Decreasing the liquid velocity somewhat delayed breakthrough and speeded saturation, resulting in a slightly sharper SDC. The experimental results were interpreted in terms of the system dispersion model, resulting in fitted curves for the three flow-rates. Sharpening of the SDCs corresponded to an increase in V_{PFR} and a decrease in V_{CSTR} (Table 1). V_{SYS} was unaffected by flow-rate.

Table 1
Results of the moment analysis and fitting of the model to the system dispersion curves

Q (ml/min)	Moment analysis V_{SYS} (ml)	Fitting	
		V^{a}_{CSTR} (ml)	V^{b}_{PFR} (ml)
0.2	11.29	1.82±0.02	9.47
1.0	11.35	3.16±0.04	8.19
5.0	11.33	4.27±0.06	7.06

[a] The fitting results are shown as the most likely parameter value ±95% confidence interval.
[b] The PFR volume is calculated from the mean parameter value using Eq. (29).

From the analysis of the SDCs, some flow non-idealities such as mixing were present at all flow-rates. This behavior was represented by the SDC model with sufficient accuracy. However, model simulations did not precisely duplicate the experimentally observed smooth transition from the zero concentration portion to the sigmoidal portion of the curve. This resulted in the simulated values falling below the experimental results near t_{BT}, and slightly above the observations in the linearly increasing portion of the curve. Nevertheless, the general trend was represented well by this simple model. Residual errors never exceeded 15%.

4.4. Adsorption breakthrough curves

BTCs were measured at three different flow-rates (Fig. 4). Solid lines represent the arithmetic mean of duplicate experiments for flow-rates of 1.0 and 5.0 ml/min, and triplicates for 0.2 ml/min. Reproducibility was a function of the slope of the BTC, i.e. the flatter the curve the closer the match between repeated experiments.

Altogether, the BTCs had in common a sigmoidal shape, but the exact shape of the curve was strongly dependent on the flow-rate. As the flow-rate increased, the BTCs transformed from a shape characterized by a broad gradual increase in concentration (0.2 ml/min) into a shape characterized by a narrow sudden increase in concentration after an initial delay time, and an abrupt transition into a

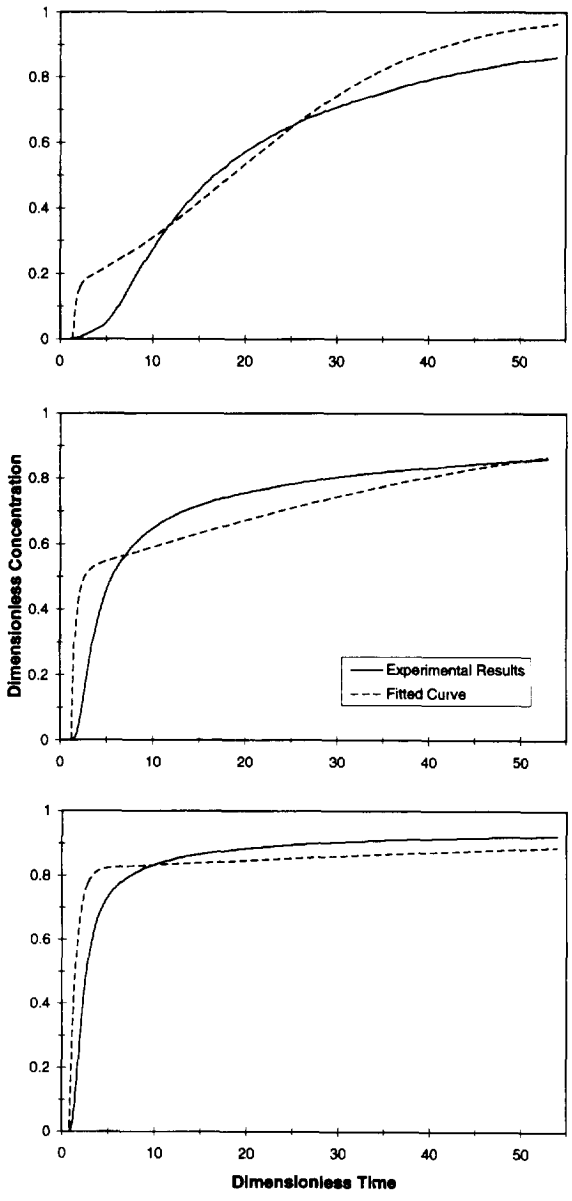

Fig. 4. Experimental breakthrough curves and fitted curve for the breakthrough curve model at flow-rates of 0.2 ml/min (top panel), 1.0 ml/min (middle panel) and 5.0 ml/min (bottom panel).

region of relative saturation. The shape of the BTCs was not due to system dispersion: as the flow-rate decreased, the BTCs broadened, whereas the SDCs sharpened. Complete saturation of the membrane was never achieved, i.e. the effluent concentration never reached the concentration of the feed solution.

4.5. Analysis of breakthrough curves using the theoretical model

In order to better evaluate the fundamental phenomena underlying the BTCs and to generalize the experimental results, the experimental data were fit to the theoretical models. The BTC model (Eq. (13)) was used as the input to the CSTR model (Eq. (30)), then the response of the CSTR model was used as the input to the PFR model (Eq. (32)). The overall solid-phase mass transfer coefficient k_{ol} was used as the sole fitting parameter (Table 2). Parameter values used in the simulations are shown in Table 3. There was a strong statistically-significant increase in k_{ol} as the flow-rate increased. The simulated BTCs, for flow-rates of 0.2, 1.0 and 5.0 ml/min (Fig. 4), were characterized by an abrupt, almost linear increase in concentration at the delay time ($\tau = \tau_{delay}$) calculated from the PFR model. In this region, the simulations generally overestimated the data. As τ approached infinity, the simulations first crossed over the experimental data, then both curves asymptotically approached complete saturation. As the flow-rate increased, the shape of the simulated and experimental curves changed in a similar manner, i.e. the BTCs broadened.

In the simulations, the sudden increase in concentration at the point of breakthrough was the result of protein that was not captured because the residence time of the liquid in the membrane was too short for protein mass transfer to the binding site. As the flow-rate increased, the fraction of protein that was not captured increased, which increased the

Table 2
Results of breakthrough curve fitting

Q (ml/min)	Re	$ReSc$	k_{ol}^{a} (cm/s)	Sh
0.2	1.4×10^{-3}	15	$9.9\pm0.6\times10^{-7}$	0.02
1.0	6.8×10^{-3}	76	$1.9\pm0.1\times10^{-6}$	0.04
5.0	3.4×10^{-2}	380	$2.8\pm0.3\times10^{-6}$	0.06

[a] The fitting results are shown as the most likely parameter value ±95% confidence interval.

Table 3
Values of the parameters used in simulating the breakthrough curves

Parameter	0.2 ml/min	1.0 ml/min	5.0 ml/min
Membrane capacity c_t (M)	2.35×10^{-3}	2.35×10^{-3}	2.35×10^{-3}
Desorption equilibrium const. K_d (M)	5.45×10^{-7}	5.45×10^{-7}	5.45×10^{-7}
Average pore size d_p (cm)	1.5×10^{-2}	1.5×10^{-2}	1.5×10^{-2}
Porosity ε	0.75	0.75	0.75
Length of membrane L (cm)	2.04	2.04	2.04
Diffusion coefficient D (cm^2/s)	6.7×10^{-7}	6.7×10^{-7}	6.7×10^{-7}
Feed concentration c_0 (M)	4.15×10^{-5}	4.15×10^{-5}	4.15×10^{-5}
Interstitial liquid velocity v (cm/s)	9.05×10^{-4}	4.53×10^{-3}	2.26×10^{-2}
System volume V_{sys} (ml)	11.3	11.3	11.3
PFR volume V_{PFR} (ml)	9.5	8.2	7.1
Concentration of adsorbed and elutable protein $c^{int}_{s,EC}$ (M)	2.1×10^{-4}	2.2×10^{-4}	1.7×10^{-4}

Concentrations of bound protein are expressed per unit of solid membrane phase (2.5 ml). The void volume of the membrane was 7.5 ml.

extent of the sudden initial rise in concentration, and slowed the rate of approach to saturation.

4.6. Elution curves

Elution of bound protein from the membrane is an important part of the total separation process, although it has received less attention than BTCs. Similar to the BTCs, the elution curves (EC) were strongly dependent on flow-rate (Fig. 5). The peak height increased by three fold as the flow-rate decreased from 5.0 to 0.2 ml/min. However, the delay time was essentially constant at $t_{delay}\approx1$. After this point, the actual elution peak emerged, followed by a broad tail lasting several membrane volumes.

The amount of protein that eluted was calculated from the area under the EC for comparison to the amount of protein that bound as calculated from integrating the breakthrough and washing curves. As the flow-rate increased, the amount of protein that eluted was essentially unchanged (Table 3), whereas the percentage of bound protein that eluted ($100\times c^{int}_{s,EC}/c^{int}_{s,BTC-WC}$) increased somewhat from 8% to 18%.

4.7. Analysis of elution curves using the theoretical model

The ECs were analyzed by using the response of the EC model (Eq. (27)) as the input to the CSTR model (Eq. (30)), then the response of the CSTR model was used as the input to the PFR model (Eq. (32)). The overall solid-phase mass transfer coefficient k_{os} and the delay time t_{delay} due to the PFR volume were used as fitting parameters in the GREG software package.

Values for k_{os} determined from the ECs (Table 4) were significantly different statistically, and increased strongly as the flow-rate increased. The fitted curves generally agreed with the experimental data (Fig. 5) in the primary characteristics of peak height, asymmetry, and flow-rate dependence. Some secondary features of the experimental data did not precisely match the simulations e.g. the rate of approach to the baseline during tailing.

Values of τ_{delay} were calculated using $\tau_{delay}=V_{PFR}/V_{void}$ ($V_{void}=7.5$ ml), and were 1.0 to 1.4 for the EC data (Table 4) compared to 0.9 to 1.3 for the SDC data (Table 1). Although this difference is negligible for most purposes, including τ_{delay} as a fitting parameter rather than using the value from the SDCs was necessary because small changes in τ_{delay} caused a significant horizontal misalignment between the fitted and experimental ECs due to the much shorter time scale for elution relative to breakthrough.

The shape of the ECs cannot be due to system dispersion: as the flow-rate increases, the ECs broaden substantially, whereas the SDCs do not. The evidence for this conclusion can be obtained from the SDC model (Eq. (35)), in which the response

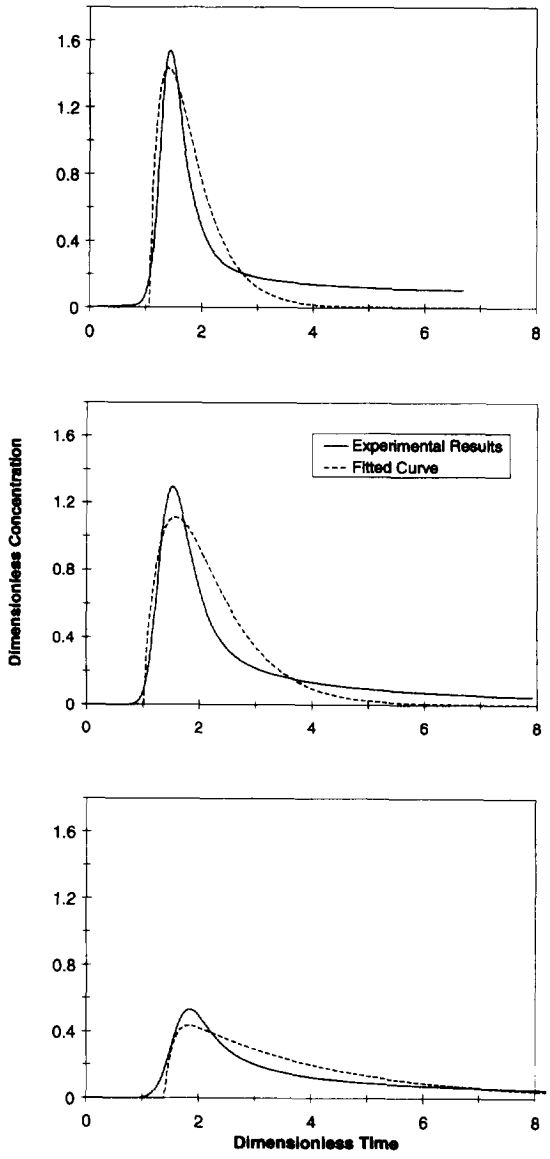

Fig. 5. Experimental elution curves and fitted curve for the elution curve model at flow-rates of 0.2 ml/min (top panel), 1.0 ml/min (middle panel) and 5.0 ml/min (bottom panel).

from the CSTR volume decays to 14% of the maximum value in two residence volumes ($2V_{CSTR}/Q$). In other words, at a dimensionless time of $\tau_{14\%} = \tau_{delay} + 2V_{CSTR}/V_{void}$, the response from the SDC model is 14% of the maximum value. At flow-rates of 0.2, 1.0 and 5.0 ml/min, values of $\tau_{14\%}$ were: 2.0, 2.0 and 1.6 using the fitted values for V_{PFR}

Table 4
Results of elution curve fitting

Q (ml/min)	k_{ol}^{a} (cm/s)	V_{PFR}^{a} (ml)
0.2	$1.4\pm0.2\times10^{-6}$	7.8±0.3
1.0	$2.6\pm0.3\times10^{-6}$	8.0±0.4
5.0	$3.6\pm0.2\times10^{-6}$	10.40±0.05

[a] The fitted results are shown as the most likely parameter value ±95% confidence interval.

from the ECs (Table 4); 1.7, 1.9 and 2.1 using the fitted values for V_{CSTR} from the SDCs (Table 1); and 2.7, 3.6 and 6.7 using the experimental ECs (Fig. 5), respectively. The response of the SDC model decayed much faster and was much less flow-rate dependent than were the experimental data. Therefore, although the SDC model was an important factor in the shape of the fitted ECs, it alone could not explain the shape and flow-rate dependence of the experimental ECs.

5. Discussion

5.1. Relative importance of mass transfer phenomena for the breakthrough curves

Up to this point, the theory and fitting procedure for calculating k_{ol} are completely general and valid for other adsorptive membranes, system designs, operating conditions and solutes. No specific mass transfer mechanisms were employed in the derivations or data analysis. Values of k_{ol} represent the lumped sum total contribution of all (as yet undefined) kinetic and mass transport phenomena. Now, using an analysis of the overall mass transfer coefficient, a specific hypothesis is proposed for the mass transfer mechanism operative in our experiments.

The overall mass transfer coefficient during the BTC is a function of the local mass transfer coefficients and the slope of the equilibrium curve [14,15]. The local mass transfer coefficients account for the individual mass transfer phenomena such as film mass transfer, solid-phase diffusion and sorption. For ion-exchange, it is generally assumed that sorption kinetics are much faster than diffusive mass transport and therefore are not the rate-limiting step. From the photomicrographs (Fig. 1), the membrane

structure consisted of large macropores and membrane walls. Although convection and film mass transfer are the likely mechanisms for protein transport to the surface of the macropores, this is not necessarily the case for protein transport into the substructure of the membrane walls. In order to account individually for mass transfer in the different regions of the membrane morphology, the overall liquid-phase mass transfer coefficient (k_{ol}) was written as the sum of the contributions by solid-phase diffusion (k_s) and film mass transfer (k_f):

$$\frac{1}{k_{ol}} = \frac{1}{k_f} + \frac{1}{m' k_s} \tag{36}$$

Here k_s and k_f are the local mass transfer coefficients, and m' is the average slope, dc_s/dc^*, of the sorption isotherm between c_s and c_{si}

$$m' = \frac{c_s - c_{si}}{c^* - c_i} \tag{37}$$

The ratio R of the terms on the right hand side of Eq. (36) is a measure of the resistance of the film relative to the solid phase:

$$R = \frac{m' k_s}{k_f} \tag{38}$$

If $R > 10$, then film mass transfer prevails, whereas solid-phase diffusion is rate limiting for $R < 0.1$.

Limits to the value of m' can be found by differentiation of c_s as expressed by Eq. (3) with respect to c^*:

$$\frac{dc_s}{dc^*} = \frac{\frac{c_l}{K_d}}{\left(1 + \frac{c^*}{K_d}\right)^2} \tag{39}$$

As a lower limit, when the membrane attains saturation, m' is set by using $c^*/K_d = c_0/K_d$ in Eq. (39). As an upper limit, for $c^*/K_d < 1$, i.e. for the linear portion of the isotherm, m' can be approximated by c_l/K_d. For our system, the limits are $0.72 \leq m' \leq 4300$. Because m' is the average slope of the isotherm, its true value is located in the middle of this range.

The relative contributions of solid-phase diffusion and film mass transfer are substantially determined by the slope of the isotherm. Therefore, for purely thermodynamic reasons, the effect of solid-phase diffusion is probably minor because the binding affinity (i.e. m') is great, which forces R to large values. Other evidence that the film mass transfer resistance dominates is that k_{ol} increases significantly with flow-rate. If solid-phase diffusion was dominant, then there would not be a flow-rate dependence. Only the theory for film mass transfer contains a flow-rate dependence [14]. Furthermore, the time scale for protein diffusion into the membrane wall ($t_s = l^2/D$) can be compared to that for overall mass transfer ($t_{ol} = d_p/k_{ol}$). From Fig. 1E, the membrane wall thickness (l) is about 10^{-3} cm, resulting in $t_s = 1.5$ s. Using values for k_{ol} from Table 2, $t_{ol} = 5 \times 10^3$ to 2×10^4 s. Therefore, for the system under investigation, it is likely that solid-phase diffusion is unimportant, and the film mass transfer resistance is dominant.

5.2. Design and operating conditions for the breakthrough curves

It is of practical value to extrapolate from the experimental results to cases with different pore size, diffusion coefficient and interstitial liquid velocity. For film mass transfer as the rate limiting mechanism, Eq. (36) simplifies to $k_{ol} = k_f$. For convective mass transfer, the Sherwood number ($k_f d_p/D$) is a function of the Reynolds and Schmidt numbers [14]. For example, for creeping flow in a packed bed of spheres ($Re < 10$), film theory [23] results in the correlation $Sh \propto (ReSc)^{1/3}$. From this, the mass transfer coefficient depends on D, d_p and v according to the relation

$$k_f \propto v^{1/3} \left(\frac{D}{d_p}\right)^{2/3} \tag{40}$$

Using this proportionality, the results of the best fit of the BTCs were extrapolated within the limits set by the condition for negligible axial dispersion, i.e. $Pe_\xi > 40$ and the validity of the film mass transfer correlation. These constraints on the extrapolation resulted in an upper and lower limiting value for the average pore size, and in an upper limiting value for the diffusion coefficient.

Fig. 6 contains the results of the simulation for variation in pore size. The BTC at a flow-rate of 5.0

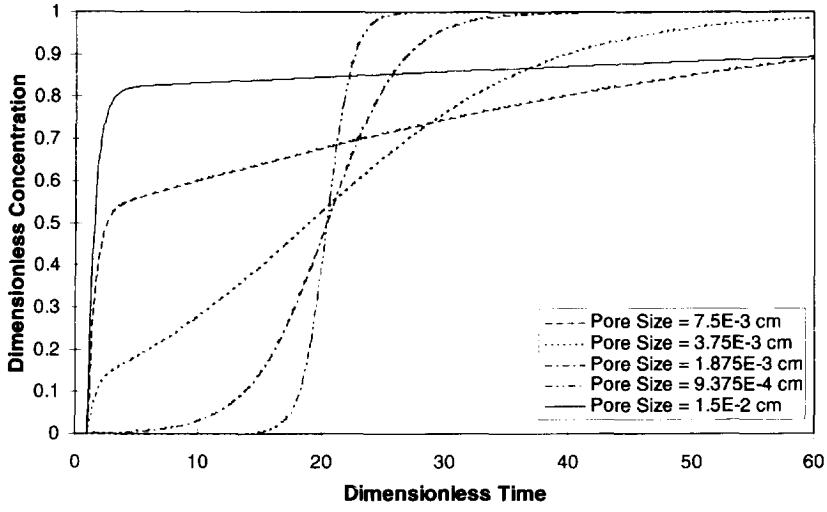

Fig. 6. Effect of pore size on sharpness, simulated using the breakthrough curve model.

ml/min is gradually transformed into the desired shape of a steep concentration front as the pore size decreased.

The problem statement can be rephrased such that instead of determining the sharpness of the BTC at different average pore sizes, the flow-rate can be calculated that produces a target sharpness for given values for d_p and D [5]. A BTC was considered to be sharp if the concentration of the solute near the exit of the membrane decreases from 70% to 10% of the feed solution concentration over a distance equal to 10% of the membrane thickness. Or, expressed mathematically

$$C = 0.7 \text{ at } \zeta = 0.9 \tag{41}$$

$$C = 0.1 \text{ at } \zeta = 1.0. \tag{42}$$

In Fig. 6, the simulated BTC for an average pore size of 9.375×10^{-4} cm meets this 70% sharpness condition.

Fig. 7 contains the result of the simulation. Each line corresponds to a different diffusion coefficient representing a specific biological molecule: alanine–glycine ($D = 7.2 \times 10^{-6}$ cm^2/s), ribonuclease A ($D = 1.26 \times 10^{-6}$ cm^2/s), BSA ($D = 6.7 \times 10^{-7}$ cm^2/s), and fibrinogen ($D = 2.0 \times 10^{-7}$ cm^2/s). Increasing the diffusion coefficient and decreasing the pore size increases the required flow-rate, i.e. decreases the required residence time. Residence times shorter than the calculated values cause broadening of the BTCs whereas longer residence times sharpen the BTC beyond the target sharpness condition.

Fig. 7 should be used for order-of-magnitude estimates only, because the mass transfer coefficients were extrapolated to pore sizes that are several orders-of-magnitude smaller than the experimental value, using a correlation developed for columns packed with beads not for microporous membranes. Furthermore, values for Sh (i.e. k_{ol}) determined from the experimental data using microporous membranes (Table 2) were much less ($\approx$0.5%) than those calculated using the theory for a packed bed of spheres [23]. In other words, $t_{ol} >> t_{film}$. This discrepancy signals that perhaps there was an additional unexplained kinetic or mass transfer resistance at play. If more than a general indication of trends is needed, then the simulations should be verified experimentally using membranes having a smaller pore size. Moreover, different ion-exchange membranes may have very different morphologies, which would strongly impact the values of the mass transfer coefficients. For example, some ion-exchange membranes have polymer tentacles grafted to the internal pore structure [24]. If the pore size of these membranes is increased, then the BTCs will be mass transfer limited and strongly dependent on flow-rate, and the tentacle layer may present a new resistance to mass transfer not considered in this work. Never-

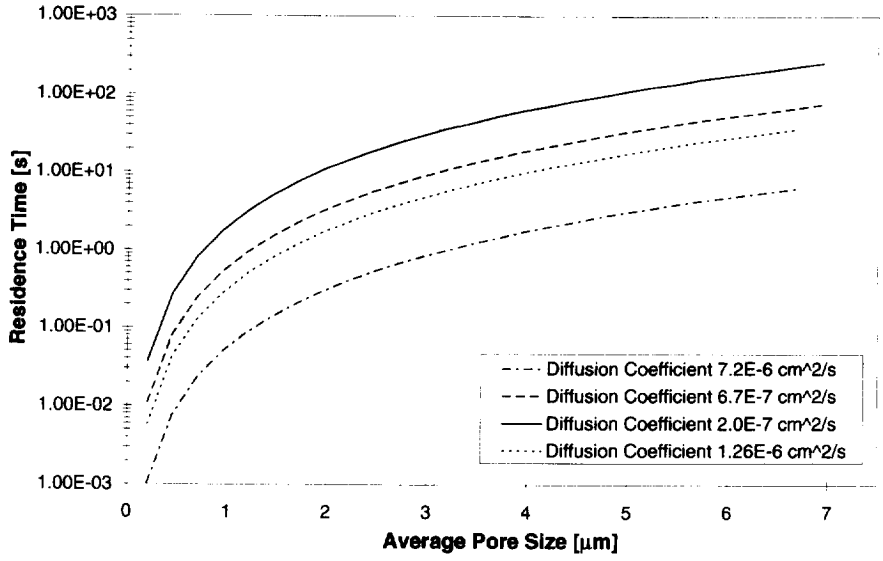

Fig. 7. Residence time in the membrane required at a given pore size to attain a sharpness condition of 70% simulated using the breakthrough curve model.

theless, the general concepts and issues identified in this work will be among the central issues in the design and operation of all large pore-size ion-exchange membrane separation systems.

5.3. Relative importance of mass transfer phenomena for the elution curves

The mechanism for protein transport during breakthrough is inverted from that during elution, i.e. for breakthrough, protein binding occurs with high affinity, and binding sites are initially unoccupied; for elution, no protein binding occurs (zero affinity), and binding sites are initially occupied. During elution, salt ions quickly diffuse into the structure of the membrane and almost instantaneously interrupt the binding interaction. Protein bound to the surface of the macropores can elute by diffusing through the film, and then into the convection pathway. Protein bound to the solid phase must first diffuse out of the solid phase, then through the film, and finally out into the convection pathway.

Because a sorption isotherm does not exist during elution, it is not possible to relate the solid and liquid phase concentrations during elution using a relationship like Eq. (36). Therefore, the method used to determine the relative importance of film mass transfer and solid-phase diffusion during breakthrough cannot be used during elution.

Instead, the relative importance of solid-phase diffusion to the overall mass transfer resistance is ascertained using the result that k_{os} increased markedly with flow-rate. If solid-phase diffusion was dominant, then k_{os} would not depend on flow-rate. Because only the theory for film mass transfer contains a flow-rate dependence, then both the BTC and EC must be controlled by the film mass transfer resistance. The conditions that sharpen the BTCs (Fig. 7) will also sharpen the ECs, e.g. decreasing the pore size and molecular size of the solute, and increasing the residence time of the liquid in the membrane.

Although there was agreement between the trends and general behavior of the simulated and experimental ECs, perfect agreement was not obtained. Perhaps this was due to some simplifying assumptions made in the model such as uniform pore size and ideal plug flow inside the membrane. Photomicrographs (Fig. 1) are clear evidence that the assumption of a single pore size is highly idealized. Furthermore, flow maldistribution will cause some of the liquid to pass through the center of the membrane cartridge faster than liquid flowing along the edges. This will cause the edges to elute later than the

center, producing tailing as observed in the experiments. Nevertheless, simulations portray the essential features of the experimental ECs and the flow-rate dependence resulting from the effects of film mass transfer limitations.

Finally, although the percentage of bound protein that was removed during elution was small (8 to 18%), all bound protein was removed by 0.2 *M* NaOH during the cleaning procedure (data not shown). BSA was not soluble at elevated concentrations or in solutions of high ionic strength. During elution, 1 *M* NaCl was added to the L/W buffer to quickly remove bound protein in a concentrated elution peak. This procedure probably caused the protein to aggregate in the pores of the membrane, trapping it there. Adjusting the pH to well above the isoelectric point of BSA (p*I*=4.7) may increase the percentage elution of bound protein because aggregates would presumably not form.

6. Conclusions

Mass transfer limitations in protein separations using ion-exchange membranes were studied in this work. A mathematical model describing the binding behavior of the protein including convection, diffusion and Langmuir sorption was developed for the loading and elution stage. It was combined with a system dispersion model consisting of a mixing and a delay volume in series to account for external mixing effects. Experiments for separation of bovine serum albumin monomer from dilute aqueous solution using a strongly acidic SP-type ion-exchange membrane having an average pore size of 150 μm were performed at three different flow-rates of 0.2, 1.0 and 5.0 ml/min and compared to simulations using the theoretical model.

BTCs and ECs exhibited a strong dependence on the flow-rate indicating that the overall system dynamics were far from equilibrium. This behavior was attributed to mass transfer resistance as the rate limiting mechanism. A calculation of the relative importance of different mass transfer mechanisms revealed that film mass transfer probably dominated the overall mass transfer resistance throughout the entire BTC and EC. For both BTCs and ECs, the simulations using the model were able to fit the general trend of the experimental observations, but failed to give a precise fit on a point-by-point basis. Possible explanations for the lack of fit may arise from the assumptions of uniform pore size, and ideal plug flow for the binding model. Furthermore, for the BTCs only, use of a constant mean value for C_s of 0.5 in Eqs. (6,7) is an approximation because it actually rises from 0.0 to 1.0 during the BTC. Although this approximation does not affect the solution to the BTC model (Eq. (13)), it does affect the values of the dimensionless time (T_L) and spatial coordinate (Z_L). Including these factors in the model may increase agreement between the simulations and experimental observations.

Effects of flow non-idealities could not be neglected in the analysis. SDCs at the three flow-rates were analyzed for flow non-idealities and the system volume. It was found that at low flow-rates, the system behavior was close to ideal plug flow, whereas flow non-idealities such as mixing were important at increased flow-rates.

Finally, the general influence of the variation of pore size and protein diffusion coefficient on the BTCs was simulated. It was found that a reduction of the pore size and a decrease in the flow-rate resulted in a sharpening of the BTC. An increase in the protein diffusion coefficient resulted in a broadening of the BTC. The flow-rate which yielded a target sharpness of the BTC was determined using the model.

The model employed in this work is a valuable tool to analyze the performance of ion-exchange membrane systems with respect to key parameters such as flow-rate, average pore size and solute diffusion coefficient in cases where mass transfer is rate limiting. In contrast to previous work, where no flow-rate effects were observed because the membrane pore size was too small, this is the first experimental characterization and theoretical analysis of mass transfer limitations in protein separations using adsorptive membranes having large pores. Moreover, the first model is presented of the pertinent mass transfer processes operative during the important process of elution from adsorptive membranes, along with an analysis of experimental data. However, further investigation is needed to refine the theoretical model and to quantify the precise contri-

bution of different limiting mass transfer mechanisms for membranes of smaller pore size.

7. Symbols

a_m	ratio of surface area to solid volume, $cm^{-1}(=6\varepsilon/d_p(1-\varepsilon))$
c	solute concentration in the liquid phase, M
c^*	solute concentration in the liquid phase in equilibrium with c_s, M
c_i	interfacial solute concentration in the fluid phase, M
c_{in}	influent concentration, M
c_{init}	initial solute concentration, M
c_l	membrane capacity based on the solid volume, M
c_{out}	effluent concentration, M
c_s	solute concentration in the solid phase based on the solid volume, M
c_s^∞	solute concentration in the solid phase in equilibrium with c_0, M
c_s^*	solute concentration in the solid phase in equilibrium with c, M
$c_{s,BTC-WC}^{int}$	concentration of total adsorbed solute in solid phase, M
$c_{s,EC}^{int}$	concentration of adsorbed and elutable solute in solid phase, M
c_{si}	interfacial solute concentration in the solid phase, M
c_0	solute concentration in feed solution, M
C	dimensionless solute concentration in the liquid phase $(=c/c_0)$
C_s	dimensionless solid-phase solute concentration, M $(=c_s/c_s^\infty$ for BTC, $=c_s/c_{s,EC}^{int}$ for EC)
d_p	average pore size of membrane, cm
D	molecular diffusion coefficient of the solute, cm^2/s
I_0	modified Bessel function of zeroth order
J	J-function defined by Eq. (14)
k_f	local film mass transfer coefficient, cm/s
k_{ol}	overall liquid-phase mass transfer coefficient, cm/s
k_{os}	overall solid-phase mass transfer coefficient, cm/s
k_s	local solid-phase mass transfer coefficient, cm/s
K_d	desorption equilibrium constant, M
l	membrane wall thickness, cm
L	length of membrane, cm
m	dimensionless saturation capacity $(=(1-\varepsilon)c_s^\infty/\varepsilon c_0$ for BTC, $=(1-\varepsilon)c_{s,EC}^{int})/\varepsilon c_0$ for EC)
m'	dimensionless slope of the adsorption isotherm
M_n	n^{th} exit moment, variable units
n	dimensionless number of transfer units $(=(1\pm\varepsilon)k_{ol}a_mL/\varepsilon v)$ or $(=(1-\varepsilon)k_{os}a_mL/\varepsilon v)$
Pe_ξ	dimensionless axial dispersion Peclet number $(=vL/\xi)$
Q	volumetric flow-rate, ml/s
r	dimensionless separation factor $(=1+c_0/K_d)$
R	dimensionless ratio of mass transfer resistances
Re	dimensionless Reynolds number $(=d_p\rho r_f/\mu_f)$
$ReSc$	dimensionless Reynolds-Schmidt number $(=\varepsilon v d_p/D)$
Sh	dimensionless Sherwood number $(=k_f d_p/D)$
t	time, s
$\bar{t}$	mean residence time, s
t_{delay}	delay time due to the PFR volume, s
t_{film}	time-scale for film mass transfer, s $(=d_p^2/4D)$
t_{ol}	time-scale for overall mass transfer, s $(=d_p/k_{ol})$
t_s	time-scale for solid-phase diffusion, s $(=l^2/D)$
t_{sys}	delay time due to the system volume, s
T_L	dimensionless time in the Thomas solution $\left(=\left(t-\frac{z}{v}\right)\frac{k_{ol}a_m c_0(K_d+c_0)}{c_s^\infty(K_d+c_0)-c_0c_s}\right)$
v	interstitial liquid velocity, cm/s
V_{CSTR}	CSTR volume, ml
V_{ext}	external volume, ml
V_{PFR}	PFR volume, ml
V_{sys}	system volume, ml
V_{void}	void volume, ml

z spatial coordinate, cm

Z_L dimensionless spatial coordinate in the Thomas solution

$$\left(= \frac{1-\varepsilon}{\varepsilon} \frac{z}{v} \frac{k_{ol} a_m c_s^{\infty} (K_d + c_0)}{c_s^{\infty} (K_d + c_0) - c_0 c_s} \right)$$

7.1. Greek letters

α argument in the J-function defined by Eq. (14)

β argument in the J-function defined by Eq. (14)

ε void fraction

ζ dimensionless spatial coordinate ($=z/L$)

η integration variable

θ dimensionless contact time ($=\tau-\zeta$)

μ_f liquid viscosity, g/(cm s)

μ_n n^{th} inlet moment, variable units

ξ axial dispersion coefficient, cm^2/s

ρ_f liquid density, g/ml

τ dimensionless time ($=vt/L$)

τ_{BT} dimensionless breakthrough time

τ_{delay} dimensionless delay time due to the PFR volume

$\tau_{14\%}$ dimensionless time for SDC model response to be $1/e^2$ of maximum value

Acknowledgments

Funding for this work was provided by the German Academic Exchange Service (Deutscher Akademischer Austauschdienst) and the Wisconsin Center for Dairy Research.

References

[1] S. Brandt, R.A. Goffe, S.B. Kessler, J.L. O'Connor and S.E. Zale, Bio/Technol., 6 (1988) 779.

[2] D.K. Roper and E.N. Lightfoot, J. Chromatogr. A, 702 (1995) 3.

[3] J. Thömmes and M.R. Kula, Biotechnol. Prog., 11 (1995) 357.

[4] W.F. Weinbrenner and M.R. Etzel, J. Chromatogr. A, 662 (1994) 414.

[5] S.-Y. Suen and M.R. Etzel, Chem. Engng Sci., 47 (1992) 1355.

[6] M.F. Zietlow and M.R. Etzel, J. Liq. Chromatogr., 18 (1995) 1001.

[7] K.G. Briefs and M.R. Kula, Chem. Engng Sci., 47 (1992) 141.

[8] J.A. Gerstner, R. Hamilton and S.M. Cramer, J. Chromatogr., 596 (1992) 173.

[9] A. Shiosaki, M. Goto and T. Hirose, J. Chromatogr. A, 679 (1994) 1.

[10] I.A. Adisaputro, Y.-J. Wu and M.R. Etzel, J. Liq. Chromatogr. and Related Techniques, 19 (1996) 1437.

[11] J.E. Kochan, Y.-J. Wu and M.R. Etzel, Ind. Eng. Chem. Res., 35 (1996) 1150.

[12] F.T. Sarfert, M.S. Thesis, University of Wisconsin, Madison, WI, 1995.

[13] S.-Y. Suen and M.R. Etzel, J. Chromatogr. A, 686 (1994) 179.

[14] A.L. Hines and R.N. Maddox, Mass Transfer. Fundamentals and Applications, Prentice Hall, Englewood Cliffs, NJ, 1985.

[15] E.N. Lightfoot, R.J. Sanchez-Palma and D.O. Edwards, in H.M. Schoen (Editor), New Chemical Engineering Separation Techniques, Interscience, New York, 1962, Ch. 2.

[16] H.C. Thomas, J. Am. Chem. Soc., 66 (1944) 1664.

[17] H.C. Thomas, Annals New York Acad. Sci., 49 (1948) 161.

[18] N.K. Hiester and T. Vermeulen, Chem. Eng. Prog., 48 (1952) 505.

[19] F.H. Arnold, H.W. Blanch and C.R. Wilke, Chem. Eng. J. 30 (1985) B9.

[20] E.N. Lightfoot, A.B. Lenhoff and R.L. Rodriguez, Chem. Eng. Sci., 37 (1982) 954.

[21] D.B. Spalding, Chem. Eng. Sci., 9 (1958) 74.

[22] W.E. Stewart, M. Caracotsios and J.P. Sørensen, General Regression Software Package for Non-Linear Parameter Estimation, GREG, Madison, WI, 1994.

[23] E.J. Wilson and C.J. Geankopolis, Ind. Eng. Chem. Fund., 5 (1966) 9.

[24] S. Tsuneda, H. Shinano, K. Saito, S. Furusaki and T. Sugo, Biotechnol. Prog., 10 (1994) 76.